Journal of Materials Chemistry A

ROYAL SOCIETY OF CHEMISTRY

PAPER

View Article Online
View Journal

Check for updates

Cite this: DOI: 10.1039/d6ta01825d

Hydronium-catching interface unlocks strongly acidic Zn metal batteries with high voltage and long-term stability

Zi-Fan He, †*abc Ting-Yu Wang,†a Ai Ling Huang,a Chi-Yu Lai,a Yi-Cheng Liao,a Shafna Kunnathumpeedika a and Chi-Chang Hu *ade

Received 2nd March 2026
Accepted 9th May 2026

DOI: 10.1039/d6ta01825d

rsc.li/materials-a

Strongly acidic aqueous batteries promise high voltage and fast kinetics but are fundamentally limited by the instability of metal negative electrodes such as Zn. Here, we demonstrate reversible Zn plating/stripping at pH = 0 by regulating the hydronium accessibility at the electrode–electrolyte interface. A defect-engineered MOF-801 coating creates a confined interfacial microenvironment, where the hydrophobic pore entrances can exclude bulk water and the defect-derived –COOH/–OH groups selectively trap hydronium. This regulation reorganizes the inner Helmholtz layer into a hydronium-depleted configuration, inducing the partial Zn^{2+} desolvation, suppressing hydrogen evolution, and homogenizing the Zn^{2+} flux. Consequently, the MOF-protected Zn symmetric cells can achieve stable cycling for longer than 1660 h at 1 mA cm^{-2} in the pH 0 electrolyte. The strategy further enables record performance in Zn–PbO_2 (2.35 V), Zn–MnO_2 (502.8 Wh kg^{-1}), and Zn-ion hybrid capacitors (30 000 cycles), extending the operational pH boundary of aqueous electrochemistry.

1 Introduction

Aqueous acidic batteries (AABs) offer promising advantages—including fast proton transport,[1] high output voltage,[2] and excellent low-temperature operation[3,4]—that can unlock energy densities unattainable in neutral or mildly acidic electrolytes. From the potential–pH diagram,[5] the redox potential of MnO_2/Mn^{2+} shifts positively with decreasing pH, while that of Zn^{2+}/Zn remains unchanged in acidic media. As a result, Zn//MnO_2 cells can deliver higher output voltages under strongly acidic conditions, contributing to increased energy density. In addition, the accelerated proton-coupled MnO_2/Mn^{2+} kinetics in acidic electrolytes further enhance both energy and rate performance. For instance, the electrolytic Zn–MnO_2 batteries in strong acidic sulfate solutions readily achieve 2.0 V output,[2] while a Prussian blue analogue (CuFe-TBA) has been reported to retain half their capacity even at 4000C in 2 M H_2SO_4.[1] However, capitalizing on these benefits requires a negative electrode that remains stable in strongly acidic environments. Although Zn is attractive due to its high capacity (820 mAh g^{-1})[6] and relatively low redox potential (−0.76 V *vs.* SHE) among aqueous-compatible metal negative electrodes (Fig. S1),[7,8] its interfacial stability rapidly deteriorates with increasing acidity.[9]

The long-standing consensus is that Zn is fundamentally incompatible with strong acids due to severe corrosion and accelerated hydrogen evolution reaction (HER; Fig. 1A).[10–12] These parasitic processes consume the active material and electrolyte, distort ion transport, and render Zn plating/stripping irreversible.[13–16] Consequently, prior strategies—such as alloying[11,12] and decoupled electrolytes[17–19]—focus on shielding Zn from acidity rather than addressing the chemical origin of instability. Recent interfacial designs capable of reversibly absorbing H^+ have extended Zn cycling to ~3600 h at pH 2.2, underscoring the importance of interface regulation.[20] Nevertheless, even the best-performing mildly acidic systems decline sharply to ~400 h at pH 1.1,[12] and reversible Zn cycling has not been achieved below pH 1. This collective trend suggests that, although stability has been extended toward stronger acidity, a fundamental boundary persists: as the pH approaches 0, Zn failure remains effectively instantaneous.

Fundamentally, Zn instability in strong acids arises not from the metal itself but from uncontrolled interfacial chemistry. Unrestricted hydronium access to the Zn surface[21,22] disrupts the inner Helmholtz layer (IHL) structure, sustains high surface hydrogen coverage, and accelerates the HER. The resulting interfacial disorder renders hydrated Zn^{2+} kinetically dominant and energetically unfavorable for uniform deposition.[23,24] These coupled processes destabilize Zn nucleation and growth, ultimately defining the practical pH boundary of reversible Zn

[a]Department of Chemical Engineering, National Tsing Hua University, Hsinchu 300044, Taiwan. E-mail: he01@imec.be; cchu@che.nthu.edu.tw
[b]Thin Film PV Technology, Imec, Imo-imomec, Thor Park 8320, Genk 3600, Belgium
[c]Energy Ville, Imo-imomec, Thor Park 8320, Genk 3600, Belgium
[d]College of Semiconductor Research, National Tsing Hua University, Hsinchu 300044, Taiwan
[e]College of Sustainability, National Tsing Hua University, Hsinchu 300044, Taiwan
† Contributed equally.

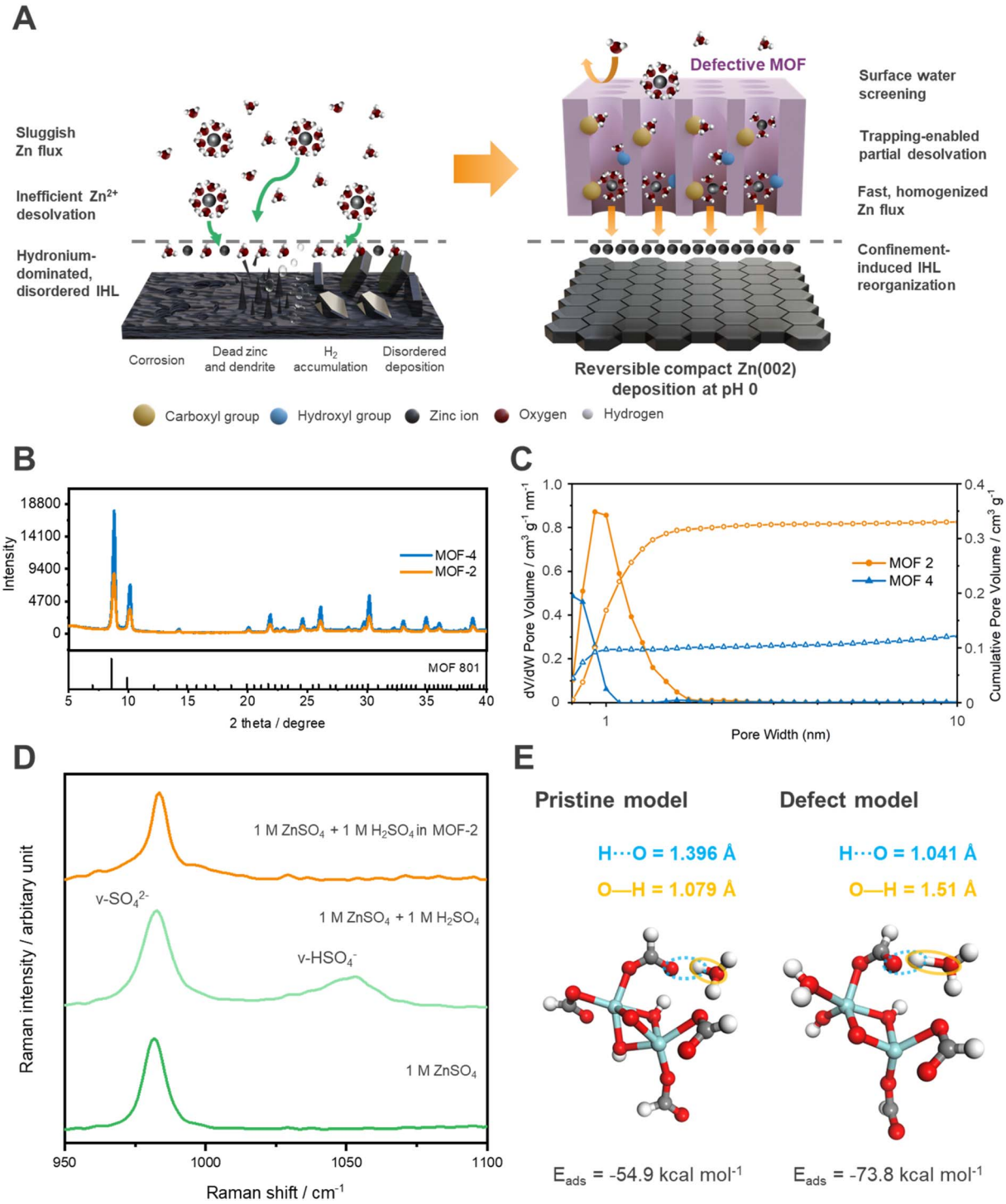

Fig. 1 Molecular design and interfacial regulation of defective MOF-801 for acidic Zn stability. (A) Schematic illustration of Zn instability under strongly acidic conditions and the defect-engineered MOF-801 strategy, which regulates interfacial accessibility by screening bulk water and selectively trapping hydronium, thereby reorganizing the inner Helmholtz layer (IHL) to favor Zn^{2+} transport. (B) XRD patterns of MOF-2 and MOF-4 confirming the preserved MOF-801 framework and defect-induced peak attenuation. (C) Pore size distributions and cumulative pore volumes from N_2 adsorption showing enlarged micropores in MOF-2 arising from missing-linker defects. (D) Raman spectra of bulk and MOF-confined electrolytes, where disappearance of the $\nu(HSO_4^-)$ signal under MOF-2 confinement indicates suppressed hydronium activity. (E) DFT analysis of hydronium interaction with pristine and defect-modified MOF-801 environments. The defective model exhibits stronger adsorption and pronounced O–H elongation with a short H···O contact, indicating enhanced proton sharing.

electrochemistry. Despite extensive efforts, a molecular strategy capable of regulating hydronium accessibility and reorganizing the IHL under strongly acidic conditions remains largely unexplored.

Here, we demonstrate that Zn metal can operate reversibly in strongly acidic electrolytes by molecularly regulating hydronium accessibility at the interface. We design a defect-engineered MOF-801 coating (MOF-2) that creates a confined interfacial microenvironment where a hydrophobic pore entrance screens bulk water and defect-derived –COOH/–OH sites selectively trap hydronium. This hydronium regulation reorganizes the inner Helmholtz layer into a hydronium-depleted, Zn^{2+}-dominated configuration, rendering fully hydrated Zn^{2+} unfavorable and inducing partial desolvation as a consequence of interfacial confinement. The resulting IHL reorganization suppresses the HER, homogenizes Zn^{2+} flux, and directs compact Zn(002) deposition, enabling stable Zn plating/stripping even at pH 0.

As a result, MOF-2 coated Zn (MOF-2@Zn) delivers long-term reversibility for 1660 h at 1 mA cm^{-2} in symmetric cells, sustains high-rate cycling at 10 mA cm^{-2}/10 mAh cm^{-2}, and unlocks full-cell voltages up to 2.35 V—among the highest reported for non-decoupled acidic Zn batteries. This hydronium-regulating principle operates universally across conversion (Zn–PbO_2), capacitive (Zn-ion hybrid capacitors), and stripping–plating (Zn–MnO_2) systems, demonstrating that hydronium control governs Zn viability in strong acid. This work establishes hydronium regulation-induced IHL reorganization as a general strategy to expand the operational pH boundary of aqueous metal batteries, opening access to strongly acidic chemistries previously considered inaccessible.

2 Results and discussion

2.1 Interfacial hydronium regulation *via* defect-engineered MOF design

Zn instability in strongly acidic electrolytes originates from a cascade of interfacial failures initiated by unrestricted hydronium access. Excessive hydronium activity disrupts the inner Helmholtz layer (IHL), accelerates hydrogen evolution, and slows down Zn^{2+} desolvation, leading to rapid corrosion and dendritic formation. As outlined in Fig. 1A, the defect-engineered MOF-801 interface is designed to intervene at this origin by regulating hydronium accessibility, thereby reorganizing the IHL and restoring reversible Zn electrochemistry under strongly acidic conditions.

To elucidate how defect chemistry governs this regulation, two MOF-801 variants—MOF-2 (high-defect) and MOF-4 (low-defect)—were synthesized using a green, low-temperature aqueous method.[25] The choice of MOF-801 is further motivated by its well-established acid stability, which enables structural integrity and interfacial functionality to be preserved in strongly acidic electrolytes.[26] Both materials retain the crystalline Zr-fumarate framework of MOF-801 (Fig. 1B),[27] but the attenuated diffraction intensity of MOF-2 indicates a higher density of missing-linker defects. Fourier transform infrared (FTIR) spectra (Fig. S2) reveal intensified –OH (3354 cm^{-1}) and –COOH (1650 cm^{-1}, 1577 cm^{-1}, and 1404 cm^{-1}) vibrations in MOF-2, confirming the enrichment of defect-associated oxygen-containing functionalities.[28,29] In MOF-801, such defects are commonly associated with the modulator (formate) coordination and missing-linker sites, which increase the population and accessibility of oxygen-based groups (*e.g.*, COO^- and OH^-) in the local coordination environment. These defect sites serve dual regulatory roles: (i) "hydronium catchers", which hydrogen-bond with H_2O/H_3O^+ and restrict their access to the Zn interface;[30,31] (ii) Zn-philic motifs possessing strongly negative electrostatic potentials (Fig. S3), favoring Zn^{2+} adsorption and guided transport within the MOF channels.[32]

Both MOFs are coated on the Zn films to form continuous and conformal interfacial layers. The linear roughness profiles measured by α-step (Fig. S4) and AFM analysis over a 5 × 5 μm^2 area (Fig. S5) show that MOF-2@Zn exhibits moderately higher surface roughness (S_a = 61.9 nm, S_z = 497.6 nm) than MOF-4@Zn (S_a = 36.0 nm, S_z = 310.7 nm). This moderate roughness variation, arising from defect-mediated MOF growth, remains limited in magnitude and does not introduce morphological discontinuities or expose the underlying Zn surface.

N_2-adsorption analysis (Fig. 1C and S6) shows that MOF-2 possesses expanded micropores (~0.9 nm) and higher pore volume, consistent with defect-induced channel widening. This increased openness enables a pore-screening effect,[27,33] where partially hydrated Zn^{2+} can enter the MOF while bulk water molecules are sterically restricted. Contact-angle measurements (Fig. S7) further support this hierarchical architecture: a relatively hydrophobic external surface limits water ingress, whereas zincophilic inner channels trap hydronium and sustain Zn ion transport. These features define a confined interfacial region that reshapes the IHL.

Raman spectroscopy provides direct molecular evidence for this hydronium regulation and IHL reorganization. In the bulk acidic electrolyte (1 M $ZnSO_4$ + 1 M H_2SO_4), the $\nu(HSO_4^-)$ band is clearly present, reflecting the hydronium-driven sulfate ionization equilibrium (eqn (1)).[34–36] In sharp contrast, this $\nu(HSO_4^-)$ signal disappears entirely in the MOF-2-confined electrolyte (Fig. 1D), demonstrating that the defective MOF channels effectively reduce the hydronium activity and create a locally hydronium-depleted microenvironment unfavorable for the HER.

$$\text{Sulfate ionization reaction: } H_3O^+ + SO_4^{2-} \leftrightarrow HSO_4^- + H_2O \quad (1)$$

To further elucidate the origin of this hydronium regulation at the molecular level, density functional theory (DFT) calculations were performed using simplified Zr_2 cluster models representing the local coordination environments of pristine and defective MOF-801 nodes (Fig. 1E, Tables S1 and S2). The pristine model is fully coordinated with formate ligands, whereas the defective model incorporates terminal OH/H_2O groups to mimic missing-linker defects and modify the local coordination environment near the defect. It should be noted that these cluster models are not intended to quantitatively reproduce the

exact formate/fumarate ratios observed experimentally, but rather to capture the local coordination changes induced by defect formation, particularly the redistribution and activation of oxygen-containing functionalities.

The calculated adsorption energies indicate that the defect-modified local environment exhibits significantly stronger interaction with hydronium than the pristine one (−73.8 *vs.* −54.9 kcal mol^{-1}). Moreover, in the optimized defective structure, one O–H bond in H_3O^+ is substantially elongated (1.51 Å), accompanied by a very short H···O distance (1.041 Å) to a formate oxygen adjacent to the defect, indicating strong proton sharing or near proton transfer. In contrast, the pristine model exhibits weaker hydrogen bonding with less pronounced O–H distortion. In addition, Hirshfeld charge analysis shows a lower residual positive charge on hydronium in the defective model (0.24) compared to the pristine model (0.43), further supporting stronger charge redistribution within the defect-associated local environment. These results suggest that defect-exposed oxygen-containing groups (COO^-/OH^--related sites) act as strong hydronium/proton-stabilizing centers, providing a mechanistic basis for the attenuation of hydronium-related Raman features.

Meanwhile, the $\nu(SO_4^{2-})$ band undergoes a characteristic blue shift under both MOF-4 and MOF-2 confinement, indicating a modified Zn^{2+} coordination environment. Deconvolution of this band (Fig. S8) reveals a marked increase in contact ion pairs (CIPs, $[Zn^{2+}(H_2O)_5\cdot OSO_3^{2-}]$),[37,38] from 62% in the bulk electrolyte to 79% in MOF-4 and 84.3% in MOF-2. The enriched CIP fraction indicates that the reorganized, hydronium-poor IHL cannot sustain solvent-separated ion pairs (SSIPs), thereby forcing partial dehydration and closer sulfate coordination.

Together, the suppression of hydronium-driven sulfate ionization, DFT-supported strong hydronium/proton stabilization, CIP enrichment, and defect-enabled confinement establish that the defective MOF-801 interphase stabilizes Zn in strong acid by regulating hydronium accessibility and reorganizing the IHL, with Zn^{2+} partial dehydration emerging because of this interfacial control. This hydronium-centered regulation forms the mechanistic foundation for the reversible Zn electrochemistry demonstrated in the following sections.

2.2 IHL-enabled long-term reversibility of Zn metal at pH 0

The hydronium-regulated interfacial environment established in Section 2.1 directly translates into markedly improved Zn reversibility under strongly acidic conditions. Fig. 2A shows that bare Zn fails rapidly in pH 0 electrolyte, exhibiting sharp voltage fluctuations due to the severe polarization and uncontrolled HER. Coating Zn with the low-defect MOF-4 extends the lifespan modestly, indicating partial mitigation of water and hydronium ingress. In contrast, MOF-2@Zn—featuring higher density of defect-derived hydronium-trapping sites—achieves 1660 h of stable plating/stripping at 1 mA cm^{-2}/1 mAh cm^{-2}, representing an excellent stability window for Zn in ultra-strong acid. The substantial improvement originates from inner Helmholtz layer (IHL) reorganization induced by hydronium regulation. By restricting hydronium accessibility and restructuring the interfacial water/proton network, the defective MOF interphase suppresses parasitic HER and stabilizes interfacial charge accumulation.

The benefits of the MOF-2 interphase become even more pronounced under high-rate operation. At 10 mA cm^{-2} and 10 mAh cm^{-2} (Fig. 2B), bare Zn fails immediately, while MOF-4 shows intermittent voltage instability. By contrast, MOF-2@Zn retains smooth and flat voltage profiles with minimal polarization, demonstrating that the hydronium-regulated IHL supports rapid interfacial charge transfer and stable Zn nucleation even under severe mass-transport stress. This rate robustness aligns with the elevated CIP fraction observed in Raman analysis, which corresponds to faster Zn^{2+} transport through partially dehydrated states.

To rationalize the excellent performance of MOF-2@Zn at high current densities, the Zn^{2+} transference number was evaluated in a neutral 1 M $ZnSO_4$ electrolyte, where the absence of excess protons enables decoupling of Zn^{2+} migration from concurrent proton conduction (Fig. S9).[39,40] MOF-2@Zn exhibits a markedly higher Zn^{2+} transference number (0.79) than bare Zn (0.51), indicating suppressed concentration polarization near the electrode. This transport advantage elevates the limiting current density (eqn (2)) and delays Sand's time (eqn (3)), explaining why MOF-2@Zn exhibits smooth voltage profiles and stable Zn plating even at 10 mA cm^{-2} and high areal capacities.[41,42]

$$J_L = \frac{2nC_0FD_{ambp}}{L(1-T^+)} \quad (2)$$

$$\tau_{Sand} = \pi D_{ambp}\left[\frac{nC_0F}{2J(1-T^+)}\right]^2 \quad (3)$$

where n is the charge number of the cation, C_0 is the bulk salt concentration, F is the Faraday constant, D_{ambp} is the ambipolar diffusion coefficient, L is the distance between the electrodes, T^+ is the transference number of cations, and J is the current density.

When benchmarked against state-of-the-art systems (Fig. 2C),[11,12,20,43,44] MOF-2@Zn operates at the upper end of the reported performance range, delivering one of the longest lifetimes for Zn symmetric cells in pH = 0 electrolytes. Notably, the MOF strategy does not rely on sacrificial additives or complex electrolytes, underscoring its intrinsic molecular-level regulation. A broader comparison with other acidic metal symmetric systems (Fig. S10)[4,45–47] further highlights the distinct advantage of the defect-engineered interphase in both stability and rate capability.

Voltage profiles across current densities (1–10 mA cm^{-2}, Fig. 2D) further confirm the stability of the MOF-2 interphase. MOF-2@Zn exhibits consistently lower and more stable overpotentials and hysteresis compared to MOF-4@Zn and bare Zn, attributable to the uniform nucleation and a persistent suppression of parasitic reactions. These results demonstrate that defect-engineered hydronium regulation enables a reorganized IHL capable of achieving the first truly reversible Zn plating/stripping in ultra-strong acidic electrolytes (pH = 0),

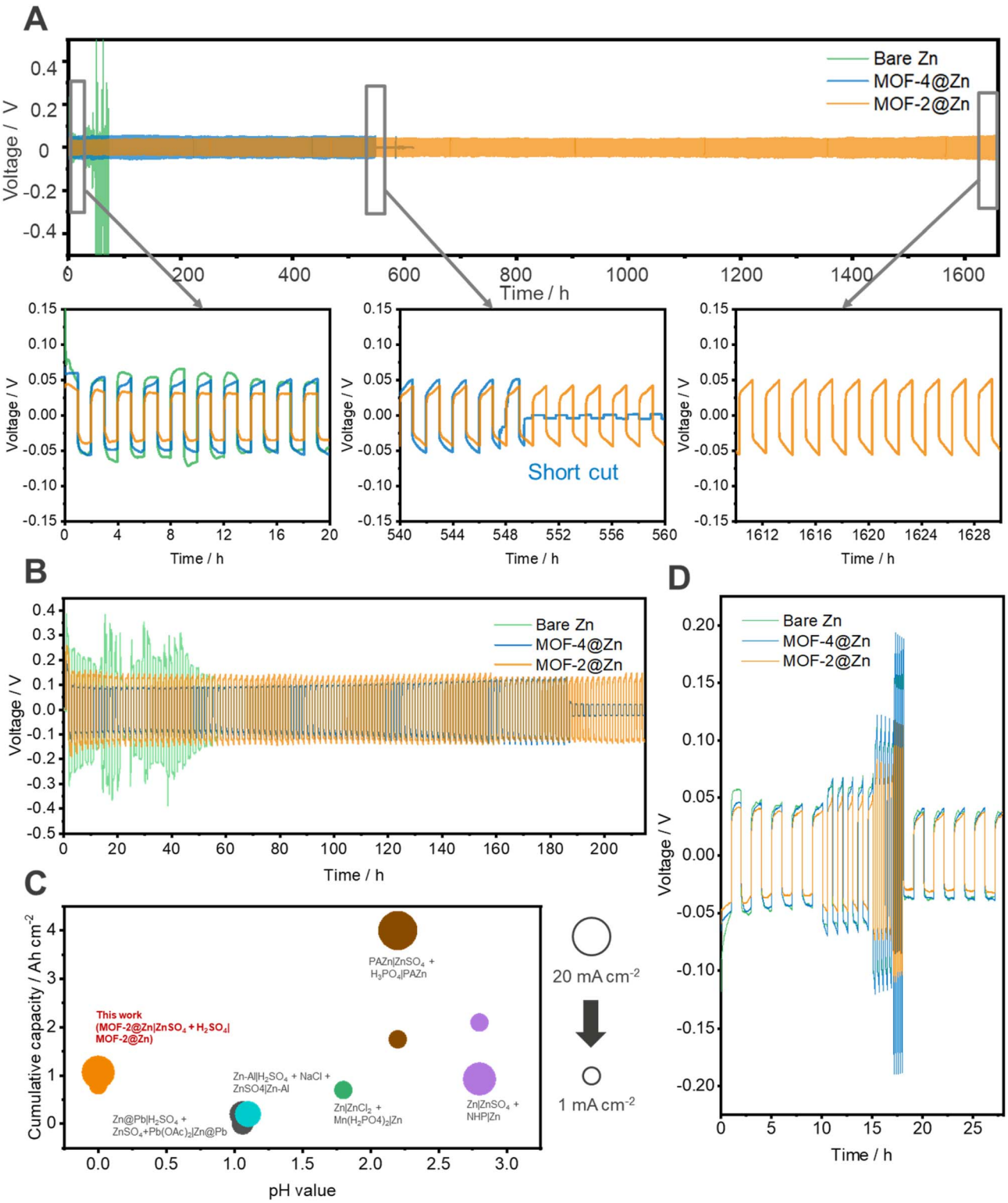

Fig. 2 Long-term reversibility and rate capability of MOF-protected Zn symmetric cells. (A) Cycling stability of bare Zn, MOF-4@Zn, and MOF-2@Zn symmetric cells operated at 1 mA cm^{-2} and 1 mAh cm^{-2}. (B) High-rate cycling at 10 mA cm^{-2} and 10 mAh cm^{-2}. (C) Electrochemical performance of the symmetric cells compared to the state-of-the-art systems in the literature.[11,12,20,43,44]. (D) Voltage profiles of these symmetric cells at various current densities (1, 2, 5, 10, and 1 mA cm^{-2}).

bridging the long-standing gap between acidic cathode chemistries and metal-anode stability.

2.3 Hydronium-regulated Zn interfaces across strongly acidic battery chemistries

To evaluate the generality of the hydronium-catcher strategy, MOF-2@Zn was integrated into three representative AAB chemistries—conversion, capacitive, and stripping–plating systems—each featuring distinct interfacial reaction pathways (Fig. 3A). Despite these fundamental differences, all three configurations share the same Zn/electrolyte interfacial challenge under strongly acidic conditions: uncontrolled hydronium access destabilizes the IHL, triggering corrosion, HER, and irreversible Zn loss. Across all systems examined, the defect-engineered MOF-2 interphase consistently stabilizes the Zn anode by regulating hydronium and reorganizing the IHL, resulting in performance metrics that rank among the best reported for strongly acidic Zn batteries (Fig. 3B and Table S4).[48–60]

2.3.1 Conversion Zn–PbO_2 batteries. The Zn–PbO_2 system represents one of the most demanding acidic battery platforms, operating in a highly corrosive electrolyte (1 M $ZnSO_4$ + 2 M H_2SO_4, pH < 0). While replacing the Pb electrode with Zn promises a lighter, higher-capacity, and more environmentally benign battery,[61,62] Zn instability has long precluded this

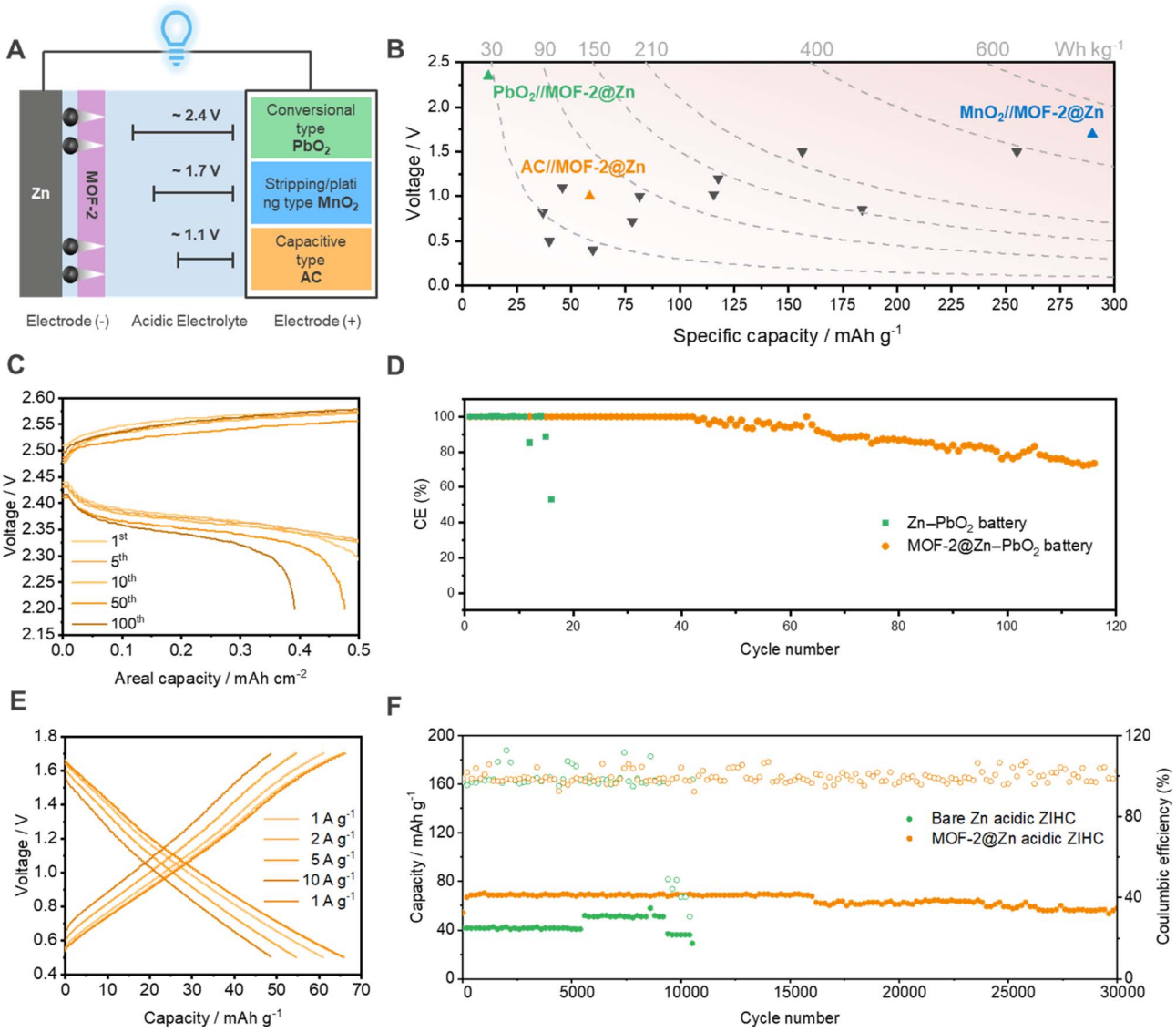

Fig. 3 Universality of the hydronium-regulating interphase across strongly acidic aqueous Zn batteries. (A) Schematic illustration of the MOF-2@Zn electrode integrated with three acidic chemistries: conversion Zn–PbO_2, capacitive ZIHC, and stripping–plating ZMABs. (B) Performance comparisons of MOF-2@Zn AABs with recent reports, plotted against the total mass of active materials of both electrodes. For the MOF-2@Zn systems, the energy and power densities are calculated using a mass-balanced configuration with an N/P ratio of 1.5. As for the literature data, values reported based on total mass are directly adopted, while those lacking such normalization are estimated using the reported N/P ratios and electrode capacities.[48–60] (C) Galvanostatic charge–discharge profiles of the MOF-2@Zn–PbO_2 battery and (D) cycling performance of bare Zn–PbO_2 and MOF-2@Zn–PbO_2 batteries with a fixed charge/discharge capacity of 0.5 mAh cm^{-2} at 4/10 mA cm^{-2}. (E) Rate performance of the MOF-2@Zn acidic Zn-ion hybrid capacitor (ZIHC) and (F) long-term cycling stability of bare-Zn and MOF-2@Zn acidic ZIHCs at 10 A g^{-1}.

chemistry. With MOF-2 protection, this limitation is fundamentally overcome. As shown in Fig. 3C–D, the MOF-2@Zn–PbO_2 battery retains >95% coulombic efficiency for 64 cycles and retains 73% of its capacity after 116 cycles, whereas the bare-Zn cell fails after only 16 cycles.

This stability is accompanied by markedly improved interfacial kinetics. The charge/discharge overpotentials drop from 75/80 mV (bare Zn–PbO_2) to 38/51 mV (MOF-2@Zn–PbO_2), indicating facilitated Zn stripping/plating kinetics under extreme acidity (Fig. 3C and S12). Remarkably, the discharge plateau reaches 2.35 V, placing it among the highest reported for non-decoupled Zn-based aqueous batteries (Fig. S13)[2,63–68] and exceeding that of commercial lead–acid batteries by ~12% (Fig. S14). These results demonstrate that hydronium regulation can fundamentally expand the electrochemical potential window accessible to Zn in strong acid.

2.3.2 Capacitive Zn-ion hybrid capacitors (ZIHCs). Strongly acidic electrolytes are widely employed in carbon supercapacitors for their ultrafast ion transport,[69,70] yet Zn-based hybrid capacitors cannot exploit these advantages due to the fast corrosion of Zn.[71,72] The hydronium-regulating MOF-2 interphase resolves this long-standing incompatibility. The acidic ZIHC assembled with MOF-2@Zn (1 M $ZnSO_4$ + 1 M H_2SO_4) displays nearly ideal triangular GCD profiles and low polarization (Fig. 3E and S15), indicative of stable capacitive behavior even at pH ≈ 0.

Compared to bare-Zn acidic ZIHCs, the MOF-2@Zn device delivers substantially improved rate capability (Fig. S16) and exceptional durability. At 10 A g^{-1}, it retains 108% of its initial capacitance and nearly 100% CE over 30 000 cycles (Fig. 3F), whereas the bare Zn device fails within 10 000 cycles. This endurance highlights that the hydronium regulation stabilizes the IHL even under rapid charge–discharge conditions, suppressing corrosion and sustaining fast interfacial charge transfer.

2.3.3 Stripping–plating Zn–MnO_2 batteries (ZMABs). Acidic ZMABs offer higher theoretical energy density by operating *via* a stripping–plating mechanism rather than proton/Zn^{2+} co-insertion. However, Zn instability has again limited their use at low pH. Using a cathode-free design (MnO_2 formed *in situ*), the MOF-2@Zn ZMAB sustains 486 stable cycles with 95.8% CE and a 1.7 V discharge plateau (Fig. S17 and S18), far outperforming the bare-Zn counterpart (176 cycles). The achieved energy and power densities, based on the total mass of active materials on both positive and negative electrodes with an N/P (negative/positive capacity) ratio of 1.5, are 502.8 Wh kg^{-1} and 5.3 kW kg^{-1}, respectively, exceeding those of most reported AABs (Fig. 3B and Table S4). These results confirm that the hydronium-regulating interphase is equally effective in high-energy stripping–plating regimes.

Overall, the consistent performance enhancement across capacitive, conversion, and plating/stripping regimes confirms that the defect-engineered MOF-2 interphase operates as a general hydronium-regulating layer that stabilizes the Zn inner Helmholtz layer. By granting Zn remarkable stability in strongly acidic electrolytes, this strategy enables high-voltage, ultra-stable, and high-energy aqueous Zn batteries that were previously considered inaccessible.

2.4 Mechanistic evidence of hydronium suppression and IHL reorganization

To elucidate how hydronium regulation and defect-assisted Zn^{2+} desolvation translate into suppressed parasitic reactions and stable Zn growth, we systematically correlate hydrogen evolution kinetics, Zn nucleation behavior, ion-transport dynamics, and deposition morphology (Fig. 4). The results reveal that hydronium confinement reorganizes the inner Helmholtz layer (IHL), which governs both reaction selectivity and Zn deposition stability under strongly acidic conditions.

HER suppression is first directly confirmed by electrochemical measurements. Linear sweep voltammetry (LSV) in 1 M H_2SO_4 shows that both MOF-coated Zn electrodes exhibit substantially reduced cathodic currents and more negative HER onset potentials compared to bare Zn (Fig. 4A), with MOF-2@Zn showing the strongest suppression. This trend is consistent with restricted hydronium accessibility at the Zn surface, in agreement with the hydronium-depleted microenvironment evidenced by Raman spectroscopy (Fig. 1D).

Tafel analysis further reveals a mechanistic shift in HER kinetics induced by the defective MOF interphase (Fig. 4B). The Tafel slope increases from 78.1 mV dec^{-1} (bare zinc) to 96.4 mV dec^{-1} (MOF-4@Zn) and 123.9 mV dec^{-1} (MOF-2@Zn), indicating progressively slower HER kinetics. Given that slopes of 120, 40, and 30 mV dec^{-1} correspond to the Volmer (eqn (4)), Heyrovsky (eqn (5)) and Tafel (eqn (6)) rate-determining steps,[73,74] bare Zn follows the Heyrovsky-limiting process dominated by rapid proton adsorption. In contrast, MOF-2@Zn transitions toward a Volmer-limited regime, indicating markedly reduced surface hydrogen coverage.[74,75] This transition indicates that hydronium trapping by the defective MOF reorganizes the IHL, thereby reducing surface hydrogen coverage and shifting HER kinetics toward a Volmer-limited regime, which effectively suppresses continuous HER under strongly acidic conditions.

$$\text{Volmer step: } H_3O^+ + e^- + M \leftrightarrow M - H + H_2O \quad (4)$$

$$\text{Heyrovsky step: } M - H + H_3O^+ + e^- \leftrightarrow H_2 + H_2O + M \quad (5)$$

$$\text{Tafel step: } 2M - H \leftrightarrow H_2 + 2M \quad (6)$$

The reconfigured IHL directly impacts Zn nucleation and growth behavior. Analysis of nucleation and quasi-steady-state deposition overpotentials[76] (Fig. 4C and S20) shows that MOF-2@Zn exhibits significantly reduced nucleation overpotentials and more stable growth plateaus compared to bare Zn. The reduced overpotentials for MOF-2@Zn indicate facilitated nucleation and sustained uniform growth enabled by homogenized Zn^{2+} flux.[77] In contrast, the drifting plateaus observed for bare Zn reflect unstable current distribution and localized surface fluctuations associated with dendritic growth.[78] Chronoamperometric responses further corroborate Zn deposition dynamics. As shown in Fig. 4D, MOF-2@Zn retains a stable current plateau with a clear 2D-to-3D transition—signatures of smooth and continuous Zn growth.[39] In contrast, bare Zn rapidly enters diffusion-limited regimes associated with uneven

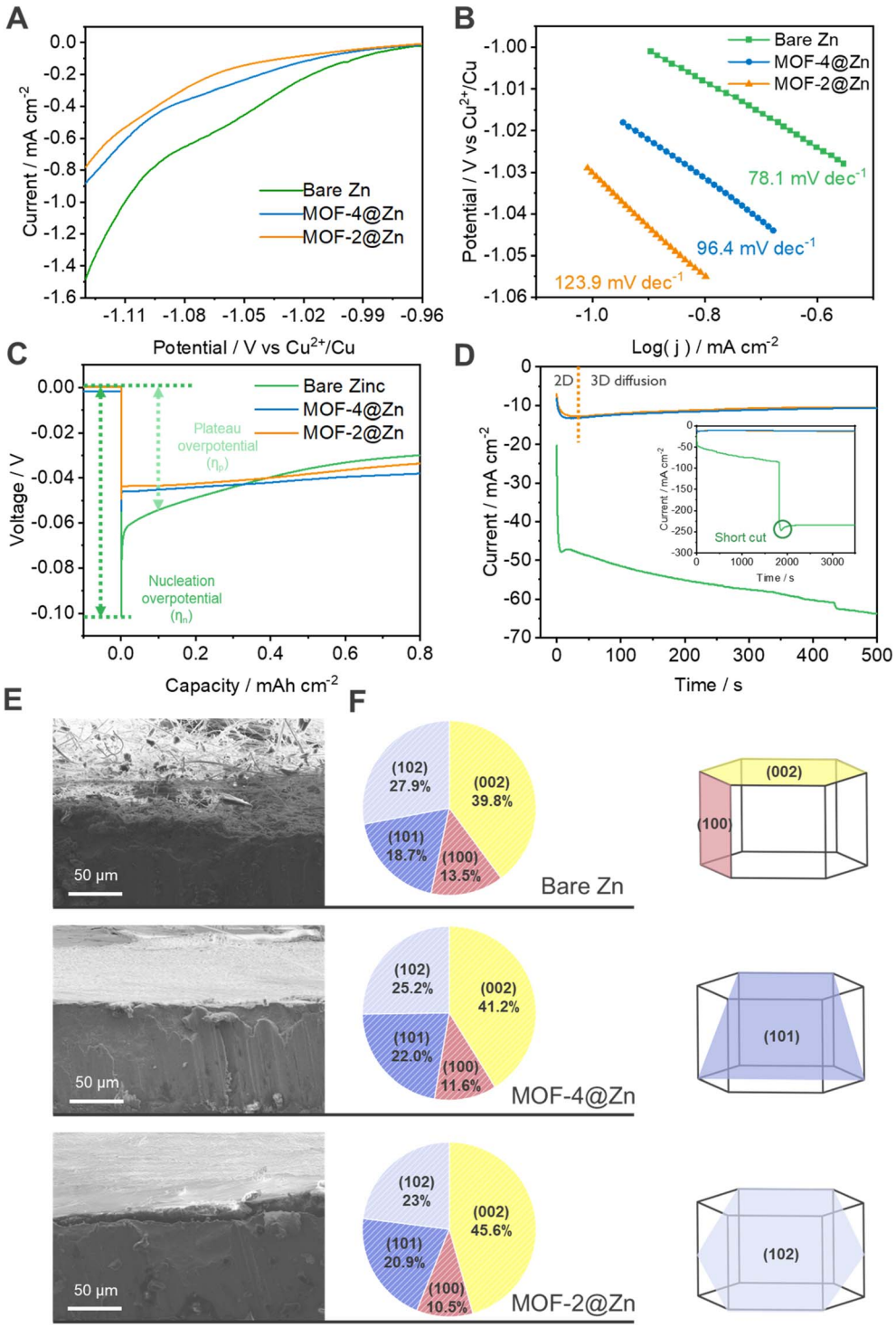

Fig. 4 Mechanistic evidence for hydronium-regulated interfacial reorganization, suppressed HER, and guided Zn deposition. (A) LSV curves in 1 M H_2SO_4 showing reduced HER currents and more negative onset potentials for MOF-coated Zn. (B) Tafel plots revealing a transition toward Volmer-limited kinetics on MOF-2@Zn, consistent with reduced surface hydrogen coverage induced by the reorganized interfacial environment. (C) Nucleation and deposition overpotentials highlighting the improved Zn nucleation behavior on MOF-protected surfaces. (D) Chronoamperometry showing a controlled 2D-to-3D transition and stable diffusion regimes for MOF-2@Zn. (E) Cross-sectional SEM of deposited Zn after 50 cycles at 1 mA cm^{-2}, revealing compact morphology on MOF-protected electrodes. (F) Relative texture coefficients showing enhanced (002)-oriented deposition and suppressed (100) growth on MOF-2@Zn after 5 cycles.

ion transport and mossy deposition. These results demonstrate that hydronium-regulated IHL restructuring mitigates current amplification and stabilizes Zn growth under acidic conditions.

Electrochemical impedance analysis confirms accelerated deposition kinetics. Room-temperature EIS measurements show reduced interfacial resistance for MOF-coated electrodes (Fig. S21), indicating improved charge-transfer and deposition dynamics. Temperature-dependent EIS further reveals a pronounced decrease in apparent activation energy for MOF-2@Zn relative to bare Zn (Fig. S22), demonstrating that the MOF interphase lowers the energetic barrier for interfacial Zn^{2+} transfer rather than merely acting as a passive barrier.

Distribution of relaxation times (DRT) analysis identifies IHL reorganization as the dominant origin of this kinetic enhancement.[79,80] As shown in Fig. S23 and S24, the high-frequency regime (10^{-4}–10^{-1} s), corresponding to fast IHL rearrangement, contributes the largest resistance under acidic conditions. This resistance exhibits a clear Arrhenius dependence (Fig. S25) and is significantly reduced for MOF-coated electrodes, particularly MOF-2@Zn, indicating facilitated IHL reorganization through hydronium trapping. In addition, a distinct low-frequency relaxation feature emerges only for MOF-coated electrodes, which we attribute to hydronium confinement and Zn^{2+} solvation-shell reorganization within the MOF channels. These confinement-induced processes homogenize Zn^{2+} transport and suppress localized ion accumulation at the interface.

The regulated interfacial dynamics are ultimately reflected in the deposited Zn morphology and crystallographic texture. Cross-sectional (Fig. 4E) and top-view (Fig. S26) SEM images after 50 plating/stripping cycles reveal dense, compact Zn layers on MOF-2@Zn, in stark contrast to the porous, mossy deposits formed on bare Zn. Texture coefficient analysis derived from XRD patterns (Fig. 4F and S27) shows a pronounced enhancement of Zn(002) orientation and suppression of Zn(100) growth on MOF-2@Zn, indicating crystallographically guided deposition. The detailed calculation procedure and formula for the texture coefficient are described in the Experimental Section of the SI. Such (002)-preferred growth, known to exhibit intrinsically low HER activity,[81–83] minimizes local current amplification and dendrite formation, thereby stabilizing long-term cycling.

Overall, these results demonstrate that hydronium confinement reorganizes the IHL, suppresses the HER, lowers Zn nucleation barriers, homogenizes ion flux, and accelerates deposition kinetics. This unified interfacial regulation mechanistically explains the exceptional reversibility observed in both Zn symmetric cells and strongly acidic full batteries, confirming that hydronium accessibility and IHL dynamics are the dominant factors governing Zn stability at pH $\approx$ 0.

3 Conclusions

Highly reversible Zn plating/stripping at pH = 0 is achieved by introducing a defect-engineered MOF-801 interphase that molecularly regulates hydronium accessibility at the Zn surface. The hydrophobic pore entrance and defect-induced –COOH/–OH groups selectively trap hydronium and exclude bulk water, thereby reorganizing the inner Helmholtz layer (IHL) into a hydronium-depleted interfacial environment. This IHL reconfiguration suppresses hydrogen evolution, lowers nucleation barriers, homogenizes Zn^{2+} flux, and promotes partial desolvation of Zn ions, leading to stable Zn deposition under ultra-strong acidic conditions.

As a result, MOF-2@Zn exhibits impressive stability, sustaining 1660 h of reversible cycling at 1 mA cm^{-2}/1 mAh cm^{-2} and retaining robust performance under deep and fast plating conditions (10 mA cm^{-2}/10 mAh cm^{-2}). The interfacial stabilization unlocks acidic Zn battery chemistries that were previously inaccessible, including a record-high 2.35 V Zn–PbO_2 cell, an ultrastable acidic ZIHC with 108% retention over 30 000 cycles, and a high-energy acidic ZMAB delivering 502.8 Wh kg^{-1}.

Overall, this work establishes hydronium regulation-induced IHL reorganization as a fundamental principle for stabilizing reactive metal electrodes in harsh acidic media. Beyond Zn, the hydronium-catcher strategy offers a general and scalable route to extending the pH limits of aqueous electrochemistry and enabling high-voltage, high-energy batteries based on other metal systems.

Conflicts of interest

The authors declare that they have no known competing financial interests or personal relationships that could have appeared to influence the work reported in this paper.

Data availability

The data supporting this article are available from the corresponding author upon reasonable request.

Supplementary information (SI): experimental details, characterization methods, computational procedures, electrochemical analysis, supplementary figures, and tables. See DOI: https://doi.org/10.1039/d6ta01825d.

Acknowledgements

The financial support of this work, by the Ministry of Science and Technology (MOST) of Taiwan under contract no. MOST 111-2221-E-007-006-MY3 and the National Science and Technology Council (NSTC) of Taiwan under contract no. NSTC 112-2221-E-007-021-MY3 and no. NSTC 114-2917-I-564-018, is gratefully acknowledged. The authors would like to thank Dr Yu-Hsiang Yang and Dr Amit Kumar Harit for their valuable suggestions on the preparation of this manuscript.

References

1 X. Wu, J. J. Hong, W. Shin, L. Ma, T. Liu, X. Bi, Y. Yuan, Y. Qi, T. W. Surta and W. Huang, *Nat. Energy*, 2019, **4**, 123–130.
2 D. Chao, W. Zhou, C. Ye, Q. Zhang, Y. Chen, L. Gu, K. Davey and S. Z. Qiao, *Angew. Chem., Int. Ed.*, 2019, **58**, 7905–7910.
3 J.-L. Yang, J.-M. Cao, X.-X. Zhao, K.-Y. Zhang, S.-H. Zheng, Z.-Y. Gu and X.-L. Wu, *EnergyChem*, 2022, **4**, 100092.

4 H. Zhang, D. Xu, F. Yang, J. Xie, Q. Liu, D.-J. Liu, M. Zhang, X. Lu and Y. S. Meng, *Joule*, 2023, **7**, 971–985.
5 C. F. Bischoff, O. S. Fitz, J. Burns, M. Bauer, H. Gentischer, K. P. Birke, H.-M. Henning and D. Biro, *J. Electrochem. Soc.*, 2020, **167**, 020545.
6 J. Gao, B. Qiu, J. Huang, J. Wen, M. Yang, P. Zhang, C. He and H. Mi, *Adv. Funct. Mater.*, 2025, **35**, 2412791.
7 Z. F. He, Y. T. Lu, T. C. Wei and C. C. Hu, *ChemSusChem*, 2023, **16**, e202300259.
8 J. Wei, P. Zhang, J. Sun, Y. Liu, F. Li, H. Xu, R. Ye, Z. Tie, L. Sun and Z. Jin, *Chem. Soc. Rev.*, 2024, **53**, 10335–10369.
9 L. Tang, H. Peng, J. Kang, H. Chen, M. Zhang, Y. Liu, D. H. Kim, Y. Liu and Z. Lin, *Chem. Soc. Rev.*, 2024, **53**, 4877–4925.
10 R. C. Salles, G. C. De Oliveira, S. L. Díaz, O. E. Barcia and O. R. Mattos, *Electrochim. Acta*, 2011, **56**, 7931–7939.
11 J. Sun, X. Zheng, K. Li, G. Ma, T. Dai, B. Ban, Y. Yuan, M. Wang, M. Chuai and Y. Xu, *Energy Storage Mater.*, 2023, **54**, 570–578.
12 P. Ruan, X. Chen, L. Qin, Y. Tang, B. Lu, Z. Zeng, S. Liang and J. Zhou, *Adv. Mater.*, 2023, **35**, 2300577.
13 A. Bayaguud, Y. Fu and C. Zhu, *J. Energy Chem.*, 2022, **64**, 246–262.
14 B. Qiu, L. Xie, G. Zhang, K. Cheng, Z. Lin, W. Liu, C. He, P. Zhang and H. Mi, *Chem. Eng. J.*, 2022, **449**, 137843.
15 H. Qin, W. Kuang, D. Huang, X. Zhang, J. Liu, L. Yi, F. Shen, Z. Wei, Y. Huang and J. Xu, *J. Mater. Chem. A*, 2022, **10**, 17440–17451.
16 N. Hu, W. Lv, H. Tang, H. Qin, Y. Zhou, L. Yi, D. Huang, Z. Wu, J. Liu and Z. Chen, *J. Mater. Chem. A*, 2023, **11**, 14921–14932.
17 C. Liu, X. Chi, Q. Han and Y. Liu, *Adv. Energy Mater.*, 2020, **10**, 1903589.
18 Y.-h. Zhu, Y.-f. Cui, Z.-l. Xie, Z.-b. Zhuang, G. Huang and X.-b. Zhang, *Nat. Rev. Chem.*, 2022, **6**, 505–517.
19 Y.-f. Cui, Z.-b. Zhuang, Z.-l. Xie, R.-f. Cao, Q. Hao, N. Zhang, W.-q. Liu, Y.-h. Zhu and G. Huang, *ACS Nano*, 2022, **16**, 20730–20738.
20 H. Yang, L. Li, D. Chen, J. Wang, Y. Tan, Z. Jiang, Y. Zhang, C. Miao, W. Zhang and W. Han, *Angew. Chem., Int. Ed.*, 2025, **64**, e202419394.
21 N. Dubouis and A. Grimaud, *Chem. Sci.*, 2019, **10**, 9165–9181.
22 C. Cheng, M. Deng, L. Li and Z. Wei, *Sci. China Chem.*, 2022, **65**, 1854–1866.
23 R. Chen, C. Zhang, J. Li, Z. Du, F. Guo, W. Zhang, Y. Dai, W. Zong, X. Gao and J. Zhu, *Energy Environ. Sci.*, 2023, **16**, 2540–2549.
24 X. Yu, M. Chen, Z. Li, X. Tan, H. Zhang, J. Wang, Y. Tang, J. Xu, W. Yin and Y. Yang, *J. Am. Chem. Soc.*, 2024, **146**, 17103–17113.
25 N. Prasetya and K. Li, *Sep. Purif. Technol.*, 2022, **301**, 122024.
26 J. Zhang, H.-J. Bai, Q. Ren, H.-B. Luo, X.-M. Ren, Z.-F. Tian and S. Lu, *ACS Appl. Mater. Interfaces*, 2018, **10**, 28656–28663.
27 H. Furukawa, F. Gándara, Y.-B. Zhang, J. Jiang, W. L. Queen, M. R. Hudson and O. M. Yaghi, *J. Am. Chem. Soc.*, 2014, **136**, 4369–4381.
28 C.-H. Liu, L. Xu, Z.-Y. Wang, S.-J. Han, Y.-B. Li, M.-L. Fu and B. Yuan, *J. Mater. Chem. A*, 2024, **12**, 31533–31546.
29 M. R. Shaik, S. F. Adil, Z. A. ALOthman and O. M. Alduhaish, *Crystals*, 2022, **12**, 151.
30 D. Xu, Z. Wang, C. Liu, H. Li, F. Ouyang, B. Chen, W. Li, X. Ren, L. Bai and Z. Chang, *Adv. Mater.*, 2024, **36**, 2403765.
31 Y. Tan, W. Xu, F. Yang, J. Tao, D. Li, Y. Zhang, F. Huang, B. Tan and H. He, *Adv. Mater.*, 2026, **38**, e22609.
32 W. Lv, J. Tao, D. Huang, J. Zhu, B. Wang, X. Yin, J. Xu and H. He, *Adv. Funct. Mater.*, 2026, **36**, e13857.
33 J. Yang, R. Zhao, Y. Wang, Z. Hu, Y. Wang, A. Zhang, C. Wu and Y. Bai, *Adv. Funct. Mater.*, 2023, **33**, 2213510.
34 W. W. Rudolph, M. H. Brooker and P. R. Tremaine, *J. Solution Chem.*, 1999, **28**, 621–630.
35 M. Li, H. Su, G. Zheng, U. Kuhn, N. Kim, G. Li, N. Ma, U. Pöschl and Y. Cheng, *Environ. Sci. Technol.*, 2022, **56**, 12863–12872.
36 J. D. Rindelaub, R. L. Craig, L. Nandy, A. L. Bondy, C. S. Dutcher, P. B. Shepson and A. P. Ault, *J. Phys. Chem. A*, 2016, **120**, 911–917.
37 X. Shi, J. Xie, J. Wang, S. Xie, Z. Yang and X. Lu, *Nat. Commun.*, 2024, **15**, 302.
38 G. Ma, L. Miao, Y. Dong, W. Yuan, X. Nie, S. Di, Y. Wang, L. Wang and N. Zhang, *Energy Storage Mater.*, 2022, **47**, 203–210.
39 H. Liu, Q. Ye, D. Lei, Z. Hou, W. Hua, Y. Huyan, N. Li, C. Wei, F. Kang and J.-G. Wang, *Energy Environ. Sci.*, 2023, **16**, 1610–1619.
40 X. Cai, W. Tian, Z. Zhang, Y. Sun, L. Yang, H. Mu, C. Lian and H. Qiu, *Adv. Mater.*, 2024, **36**, 2307727.
41 P. Bai, J. Li, F. R. Brushett and M. Z. Bazant, *Energy Environ. Sci.*, 2016, **9**, 3221–3229.
42 X. Liu, G. Wang, Z. Lv, A. Du, S. Dong and G. Cui, *Adv. Mater.*, 2024, **36**, 2306395.
43 W. Zhang, Y. Dai, R. Chen, Z. Xu, J. Li, W. Zong, H. Li, Z. Li, Z. Zhang and J. Zhu, *Angew. Chem., Int. Ed.*, 2023, **62**, e202212695.
44 Y. Liu, Z. Qin, X. Yang, J. Liu, X.-X. Liu and X. Sun, *ACS Energy Lett.*, 2022, **7**, 1814–1819.
45 D. Xu, H. Zhang, J. Xie, L. Zhou, F. Yang, J. Ma, Y. Yu, G. Wang and X. Lu, *Adv. Mater.*, 2024, **36**, 2408067.
46 Z. Yu, Q. Wang, Y. Li, F. Zhang, X. Ma, X. Zhang, Y. Wang, J. Huang and Y. Xia, *Joule*, 2024, **8**, 1063–1079.
47 X. Li, Y. Tang, C. Han, Z. Wei, H. Fan, H. Lv, T. Cai, Y. Cui, W. Xing and Z. Yan, *ACS Nano*, 2023, **17**, 5083–5094.
48 H. Jiang, W. Shin, L. Ma, J. J. Hong, Z. Wei, Y. Liu, S. Zhang, X. Wu, Y. Xu and Q. Guo, *Adv. Energy Mater.*, 2020, **10**, 2000968.
49 F. Yue, Z. Tie, S. Deng, S. Wang, M. Yang and Z. Niu, *Angew. Chem., Int. Ed.*, 2021, **60**, 13882–13886.
50 L. Tong, Y. Jing, R. G. Gordon and M. J. Aziz, *ACS Appl. Energy Mater.*, 2019, **2**, 4016–4021.
51 M. Zhu, L. Zhao, Q. Ran, Y. Zhang, R. Peng, G. Lu, X. Jia, D. Chao and C. Wang, *Adv. Sci.*, 2022, **9**, 2103896.
52 C. Strietzel, M. Sterby, H. Huang, M. Strømme, R. Emanuelsson and M. Sjödin, *Angew. Chem., Int. Ed.*, 2020, **59**, 9631–9638.

53 J. Qiao, M. Qin, Y.-M. Shen, J. Cao, Z. Chen and J. Xu, *Chem. Commun.*, 2021, **57**, 4307–4310.
54 R. Emanuelsson, M. Sterby, M. Strømme and M. Sjödin, *J. Am. Chem. Soc.*, 2017, **139**, 4828–4834.
55 Z. Guo, J. Huang, X. Dong, Y. Xia, L. Yan, Z. Wang and Y. Wang, *Nat. Commun.*, 2020, **11**, 959.
56 T. Sun, H. Du, S. Zheng, J. Shi and Z. Tao, *Adv. Funct. Mater.*, 2021, **31**, 2010127.
57 L. Yan, J. Huang, Z. Guo, X. Dong, Z. Wang and Y. Wang, *ACS Energy Lett.*, 2020, **5**, 685–691.
58 X. Wang, J. Zhou and W. Tang, *Energy Storage Mater.*, 2021, **36**, 1–9.
59 L. Zhou, L. Liu, Z. Hao, Z. Yan, X.-F. Yu, P. K. Chu, K. Zhang and J. Chen, *Matter*, 2021, **4**, 1252–1273.
60 Y. Liang, Y. Jing, S. Gheytani, K.-Y. Lee, P. Liu, A. Facchetti and Y. Yao, *Nat. Mater.*, 2017, **16**, 841–848.
61 T. Gao, Y. Sun, L. Gong, C. Ma, J. Wang and L. Su, *J. Electrochem. Soc.*, 2020, **167**, 020552.
62 P. Leung, Q. Xu and T. Zhao, *Electrochim. Acta*, 2012, **79**, 117–125.
63 Q. Ni, H. Jiang, S. Sandstrom, Y. Bai, H. Ren, X. Wu, Q. Guo, D. Yu, C. Wu and X. Ji, *Adv. Funct. Mater.*, 2020, **30**, 2003511.
64 T. Sun, Q. Nian, S. Zheng, J. Shi and Z. Tao, *Small*, 2020, **16**, 2000597.
65 R. Trócoli and F. La Mantia, *ChemSusChem*, 2015, **8**, 481–485.
66 Y. Lu, J. Wang, S. Zeng, L. Zhou, W. Xu, D. Zheng, J. Liu, Y. Zeng and X. Lu, *J. Mater. Chem. A*, 2019, **7**, 21678–21683.
67 L. Zhang, L. Chen, X. Zhou and Z. Liu, *Sci. Rep.*, 2015, **5**, 18263.
68 L. Ma, S. Chen, H. Li, Z. Ruan, Z. Tang, Z. Liu, Z. Wang, Y. Huang, Z. Pei and J. A. Zapien, *Energy Environ. Sci.*, 2018, **11**, 2521–2530.
69 L. Tang, X. Ji, P. Wu, H. Luo, Y. Zhu, L. Deng, S. Cheng and M. Liu, *Electrochim. Acta*, 2020, **353**, 136562.
70 A. Mendhe and H. Panda, *Discov. Mater.*, 2023, **3**, 29.
71 Z. Hou, L. Chang, W. Yang, R. Yang, A. Wei, K. Cai and S. Luo, *J. Energy Storage*, 2024, **100**, 113550.
72 L. Yu, J. Li, N. Ahmad, X. He, G. Wan, R. Liu, X. Ma, J. Liang, Z. Jiang and G. Zhang, *J. Mater. Chem. A*, 2024, **12**, 9400–9420.
73 L. Miao, Z. Xiao, D. Shi, M. Wu, D. Liu, Y. Li, X. Liu, Y. Sun, S. Zhong and Z. Qian, *Adv. Funct. Mater.*, 2023, **33**, 2306952.
74 F. Bao, E. Kemppainen, I. Dorbandt, R. Bors, F. Xi, R. Schlatmann, R. van de Krol and S. Calnan, *ChemElectroChem*, 2021, **8**, 195–208.
75 T. Shinagawa, A. T. Garcia-Esparza and K. Takanabe, *Sci. Rep.*, 2015, **5**, 13801.
76 H. Liu, Y. Zhang, C. Wang, J. N. Glazer, Z. Shan and N. Liu, *ACS Appl. Mater. Interfaces*, 2021, **13**, 32930–32936.
77 Y. Li, C. B. Musgrave III, M. Y. Yang, M. M. Kim, K. Zhang, M. Tamtaji, Y. Cai, T. W. Tang, J. Wang and B. Yuan, *Adv. Energy Mater.*, 2024, **14**, 2303047.
78 Y. Shang and D. Kundu, *Batter. Supercaps*, 2022, **5**, e202100394.
79 Y. Wang, T. Wang, Y. Mao, Z. Li, H. Yu, M. Su, K. Ye, D. Cao and K. Zhu, *Adv. Energy Mater.*, 2024, **14**, 2400353.
80 Y. Yao, X. Zhao, G. Chang, X. Yang and B. Chen, *Sml Struct.*, 2023, **4**, 2200187.
81 C. Fan, W. Meng, J. Han, T. Li, D. Zuo, S. Deng, D. Li and L. Jiang, *Energy Storage Mater.*, 2024, **71**, 103554.
82 M. Zhou, S. Guo, J. Li, X. Luo, Z. Liu, T. Zhang, X. Cao, M. Long, B. Lu and A. Pan, *Adv. Mater.*, 2021, **33**, 2100187.
83 T.-Y. Wang, H.-Y. Huang, Y.-H. Tu, Y.-C. Liao, C.-Y. Lai, T. Jacob, M. M. Elnagar, M. Al-Shakran and C.-C. Hu, *Mater. Horiz.*, 2026, DOI: 10.1039/D6MH00367B.